

Small Angle X-ray Scattering (SAXS) with Synchrotron Radiation Sources

Stefano Polizzi and Francesco Spinozzi

Abstract This is not a treatise on small angle scattering; it is a presentation of the application of small angle scattering and the potentialities of synchrotron sources where conventional sources prove limited. A brief introduction describing the technique aims to provide the reader with no more than the qualitative tools necessary to understanding the case studies discussed further on. For a more thorough discussion, the reader is referred to standard texts in the field.

1 The physical phenomenon

When an X-ray beam passes through matter, the main effect, known as *Thomson scattering* or *elastic scattering*, is the interaction between the electric field of the incident wave and the electrons, which causes the electrons to oscillate at the same frequency as that of the wave. In turn, these oscillating charges give rise to coherent secondary electromagnetic waves with the same wavelength as that of the incident beam. The *scattering vector* \mathbf{q} , which represents the *momentum transfer*, is defined as the difference between the wave vectors of the scattered (\mathbf{k}) and the incident (\mathbf{k}_0) beam. In the case of elastic scattering these vectors have the same modulus. As a consequence the modulus of the scattering vector is $q = 4\pi \sin \theta / \lambda$, λ being the X-rays wavelength and 2θ the scattering angle. The subject of this lesson is the analysis of interferences at small angles among these secondary waves.

Stefano Polizzi

Dipartimento di Scienze Molecolari e Nanosistemi, Università Ca' Foscari, Venezia (Italy), e-mail: polizzi@unive.it

Francesco Spinozzi

Dipartimento di Scienze della Vita e dell' Ambiente, Università Politecnica delle Marche, Ancona (Italy), e-mail: f.spinozzi@univpm.it

Table 1 Objects ‘seen’ by SAXS at different angles and wavelengths.

| Wavelength [nm] | Probed dimension | |
|--------------------|------------------|-------------------|
| | 1° | 0.1° |
| 0.15 | 4.4 nm | 44 nm |
| 0.23 | 6.8 nm | 68 nm |
| ... | ... | ... |
| 400 | 11 μm | 110 μm |

1.1 Why small angles?

All scattering phenomena are ruled by a reciprocal law (through a Fourier transform): the larger the irradiated object, the smaller the scattering angle (if the wavelength of the incident radiation is constant). In other words, as we approach the angle of “zero” (the direction of the incident beam in a transmission experiment), the dimensions we are exploring grow increasingly large.

1.2 How small is “small”?

According to Bragg’s law, $\lambda = 2d \sin \theta$, the probed dimension d at a given angle 2θ and wavelength λ is of the order of $\lambda/(2\theta)$ ($\sin \theta \approx \theta$ for small angles). Let us refer to Tab. 1.2 and consider common copper radiation ($\lambda = 0.15$ nm, corresponding to about 8 keV). At one degree (0.017 radian) from the direction of the incident beam, the probed dimension is 4.4 nm. If we can measure the scattering at an angle as small as one tenth of a degree, then we can investigate objects the size of 44 nm. By using the less energetic chromium radiation ($\lambda = 0.23$ nm, about 5.4 keV) at the same angles, we can obtain information on objects of approximately 7 nm and 70 nm, respectively. Using visible radiation in the hundreds nanometer scale, we can even determine dimensions on a micrometric scale. Therefore, if we can manage to measure the scattered intensity at angles smaller than one degree, then we have a tool that will also cover the intermediate scale ranging between the atomic/molecular resolution of X-ray diffraction and the resolution of an optical microscope. In the 1920s, Wolfgang Ostwald referred to what we now call colloidal dimensions as “the world of neglected dimensions” because of the lack of experimental techniques that would cover it.

The development of small angle scattering started in the early 1930s and it continues to provide essential or, at least, complementary information, despite the large number of different experimental techniques that have since been developed. The most important technique covering the dimensional range investigated by small angle scattering is transmission electron microscopy (TEM), which can provide a di-

rect and detailed image of the sample. However, the resulting TEM image is so tiny¹ that it is extremely difficult to glean statistically significant average information on the sample. This is where SAXS comes in. The two techniques are complementary: TEM needs SAXS to obtain a significant sampling and make quantitative statements; and SAXS needs TEM for clues about the shape of particles for use in data analysis (see below). SAXS also has a great advantage over TEM: there are no artifacts in sample preparation. SAXS can even investigate wet samples or solutions - an asset when studying biological samples. To cite one example, it has been shown that the protein KLH (Keyhole Limpet Hemocyanin), used in bladder cancer treatment, has a more compact structure in its natural wet state than it does when observed by TEM [2].

1.3 What is an “object” for SAXS?

Since the incoming electromagnetic radiation interacts with the electrons, what SAXS “sees” as objects are the spatial variations in the electronic density inside the irradiated portion of matter. The electronic density difference is also called contrast, because the greater its value, the higher the scattering intensity. The meaning of electronic density variation is best explained by citing some examples.

The simplest case is that of a homogeneous particle (a portion of matter with a constant electronic density) dispersed in a matrix (a medium with a different electronic density). Consider a macromolecule in a solvent, or a crystal phase-separated in a glass by thermal treatment, or pores in porous material. Yet, what does constant electronic density mean? On an atomic scale, the electronic density continuously varies from higher values in the neighborhood of atomic positions to lower values in the space between atoms. We learned that dimensions explored by small angle scattering are larger than a few nanometers, which implies that *SAXS is not sensitive to electronic density fluctuation on an atomic scale* and that a portion of matter of homogeneous composition is perceived as a homogeneous particle, *i.e.* a particle with constant electronic density. *This means that both amorphous and crystalline particles and even voids (pores, blisters, cracks or crazes) in an otherwise homogeneous material give rise to an electronic density contrast and are detectable by small angle scattering.*

1.3.1 Single particle scattering

The scattering of a single particle in a matrix is simply its squared Fourier transform. In other words, it is related to the Fourier transform of a function that describes the particle shape and assumes, inside and outside the particle, two different yet constant electron density values. More formally, we define the *form factor* of a single parti-

¹ Williams & Carter [1] estimated that all TEMs, since they first became available up to the publishing date of their book (1996), have only examined 0.3 mm³ of material.

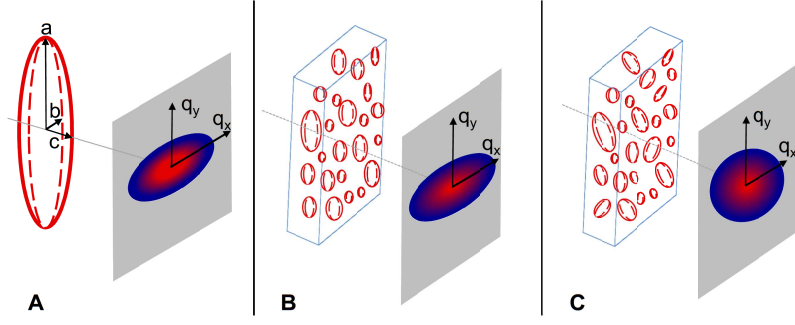


Fig. 1 Panel A: scattering of a single ellipsoidal particle. Panel B: scattering of a group of ellipsoidal particles all oriented in the same direction. Panel C: scattering of a group of randomly oriented ellipsoidal particles of different sizes.

cle dispersed in a matrix with constant electron density ρ_0 as the squared Fourier transform of the difference between the electron density of the particle, $\rho_P(\mathbf{r})$, and ρ_0 ,

$$P(\mathbf{q}) = \left| r_e \int [\rho_P(\mathbf{r}) - \rho_0] e^{i\mathbf{q}\cdot\mathbf{r}} d\mathbf{r} \right|^2, \quad (1)$$

r_e being the classical radius of the electron ($r_e = 2.8 \cdot 10^{-13}$ cm). The Fourier transform can be calculated analytically for a large number of homogeneous shapes. For example, the form factor of an ellipsoidal particle with the semi-axes a, b and c oriented along the directions x, y, z and interacting with an X-ray beam propagating along the z axis is

$$P_{\text{ell}}(\mathbf{q}) = (r_e \Delta \rho)^2 \left(\frac{4}{3} \pi abc \right)^2 \left(3 \frac{\sin \phi - \phi \cos \phi}{\phi^3} \right)^2 \quad (2)$$

where $\phi = \sqrt{a^2 q_x^2 + b^2 q_y^2}$ and q_x, q_y are the components the scattering vector (see Fig. 1A). The first factor on the right hand side of this equation contains the contrast, that is, the electronic density difference between particle and matrix; the second factor is the volume of the ellipsoid; and the third factor is a bivariate function, a surface, whose contour lines have an ellipsoidal shape oriented perpendicularly to the particle. This last statement is a consequence of the aforementioned reciprocal law between the scattering object and its scattering pattern, or between a function and its Fourier transform. Notice that since at small angles the component of the scattering vector parallel to the beam, q_z , is negligible when compared to the other components q_x and q_y , the corresponding semi-axis c does not enter into the equation of the scattering intensity: in other words SAXS experiments on oriented particles cannot “see” characteristic distances along the beam direction. A line section of the

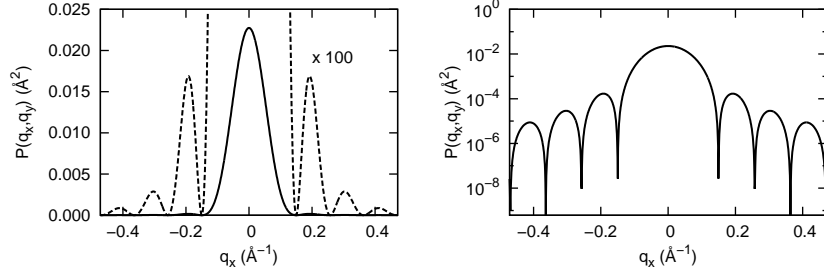


Fig. 2 Left: form factor of an oriented ellipsoidal particles at $q_y = 0$ (Eq. 2: $r_e \Delta \rho = 3 \cdot 10^{-6} \text{ \AA}^{-2}$, $a = 30 \text{ \AA}$, $b = c = 20 \text{ \AA}$). Right: same data in logarithmic scale.

scattering pattern (see Fig. 2) shows what would be observed with a linear detector: a central peak with a series of rapidly damped peaks of much smaller intensity.

1.3.2 Groups of particles

Dilute systems

When many particles are present and their reciprocal distances are large in comparison to their average size (called a dilute system), the total scattering intensity is the simple sum of the scattering of each single particle. In the case of N identical and oriented particles in a sample volume V , the result of a SAXS measurement is the so-called *macroscopic differential scattering cross section* (often referred to as *scattering intensity*),

$$I(\mathbf{q}) = nP(\mathbf{q}), \quad (3)$$

where $n = N/V$ is the so-called particle number density. This equation clearly shows that SAXS profiles are proportional to the concentration of particles.

When, however, the oriented particles have the same kind of shape but different sizes (see Fig. 1B), in order to describe the resulting scattering intensity, we must multiply the form factor (Eq. 1) by the distribution of sizes (a function that describes the frequency of the sizes of the various particles) and integrate over the whole size dimensional range. For example, the scattering intensity of a group of parallel ellipsoidal particles is given by:

$$I(\mathbf{q}) = n \int D(a, b) P_{\text{el}}(\mathbf{q}) da db \quad (4)$$

where, in this case, the distribution is expressed as a function of the two semi-axes of the ellipsoid, the two parameters which control the dimensions of the particles. Owing to the presence of particles with different sizes, the secondary peaks found in

the case of identical particles (see Fig. 2) are dampened, resulting in a monotonous decreasing curve. This is because particles with different dimensions give rise to secondary peaks at different positions; and unless the size distribution is very narrow, they cancel one another out.

In general, if the orientation of the particles vary, or if their orientation changes over time, a distribution of directions should be also introduced (see Fig. 1C). However, in the simplest case of random orientation, the scattering intensity can be simply obtained by averaging the form factor over all the possible orientations of the scattering vector,

$$I(q) = nP(q) = \frac{1}{4\pi} \int_0^{2\pi} d\alpha \int_0^\pi \sin\beta d\beta P(\mathbf{q}) \quad (5)$$

α and β being the polar angles of \mathbf{q} . Obviously, in this case, the information on particle shapes and dimensions is mixed, and one needs to make assumptions about their shape or size distribution. For example the form factor of an ellipsoidal particle randomly oriented is,

$$P_{\text{ell}}(q) = (r_e \Delta\rho)^2 \left(\frac{4}{3} \pi abc \right)^2 \times \frac{2}{\pi} \int_0^{\frac{\pi}{2}} d\alpha \int_0^{\frac{\pi}{2}} \sin\beta d\beta \left(3 \frac{\sin\phi - \phi \cos\phi}{\phi^3} \right)^2 \quad (6)$$

where $\phi = q \sqrt{(a^2 \sin^2 \alpha + b^2 \cos^2 \alpha) \sin^2 \beta + c^2 \cos^2 \beta}$. Notice that, unlike the case of oriented ellipsoids (Eq. 2), ϕ depends on all the three semi-axes. The scattering intensity only depends on the modulus of the scattering vector: the image recorded in the two-dimensional detector will show a circular symmetry around the beam centre position and all the detector counts into the pixels at the same distance from the beam center can be added. This procedure, known as *radial average*, will greatly improve the data statistics. The isotropic orientation of the particles reduces the two-dimensional SAXS intensity to a monotonous decreasing curve that cannot be associated with a unique particle size and shape.

Densely packed systems

When particles are close one to another (as in the case of solid state polymers), an additional contribution to the recorded intensity sums up with the single particle intensity; this is due to the combination between scattered beams coming from pairs of distinct particles. In such cases, the form factor should be multiplied by a term called *measured structure factor*,

$$I(\mathbf{q}) = nP(\mathbf{q}) S_M(\mathbf{q}). \quad (7)$$

If the distances between particles have some degree of regularity, they cause a constructive interference similar to the Bragg peaks characteristic of diffraction phenomena (a maximum of intensity also known as a “long period”). The explicit expressions of $S_M(\mathbf{q})$ for monodisperse or polydisperse systems are beyond the scope of this text. However, a deep interpretation of $S_M(\mathbf{q})$ may require a model of interaction among particles that accounts for both short-range and long-range forces. There is a broad range of cases that show the presence of a measured structure factor: starting with the simple case of a single maximum (long period) superposed on a monotonous decreasing trend typical of many synthetic polymers and resulting from the regular folding of long polymeric chains to form so-called micelles; on to the case of natural macromolecules, such as tendons or cellulose, in which a highly ordered, layered structure generates a number of decreasing peaks at regular distances (i.e. with a long period and higher orders); and closing with the case of proper macromolecular crystals having such a large unit cell-edge that their diffraction peaks may only be found in the small angle range.

Concentrated solutions of particles (such as macromolecules or nanoparticles) are typical examples of systems constituted by randomly oriented particles whose positions are, on average, determined by a complex interplay of interactions. The scattering intensity is usually written by taking the isotropic average of Eq. 7. In the case of a mixture of different kind of particles, it can be shown that the isotropic measured structure factor, $S_M(q)$, is a combination of the structure factors $S_{ij}(q)$ between the particles of kind i and j , which are defined as the Fourier transform of the corresponding radial correlation function,

$$S_{ij}(q) = \delta_{ij} + 4\pi(n_i n_j)^{1/2} \int_0^\infty r^2 [g_{ij}(r) - 1] dr \quad (8)$$

where r describes radial distances and δ_{ij} is the Kronecker delta function. The reader can refer to the Further Reading section for a detailed description of definitions and properties of $g_{ij}(r)$.

2 Data analysis

To sum up, we have seen that SAXS data contain information on the shapes and sizes of particles, as well as the correlations between them. In general, the information is muddled, making it impossible to separate the three different contributions without the aid of external information, such as a fixed particular shape, a certain distribution, the absence of inter-particle scattering or other detailed assumptions. Data handling procedures of small angle scattering can be roughly divided into two classes: the first includes methods that attempt to retrieve information on particles by processing the experimental data by means of appropriate mathematical transforms that do not assume specific particle shapes; the second, methods that, on the contrary, start from some assumptions regarding the form factor of the particles and the structure factor of the system, calculate the scattering intensity and try to fit it to

the experimental data by optimising several parameters. A large number of mathematical methods have been developed for both strategies, but a detailed description of them is beyond the scope of this lesson. Bear in mind, however, that in many situations, partial information can be obtained without necessarily resorting to complex mathematical transforms by making detailed assumptions and limiting the analysis to a particular angular zone, or by using suitable integral quantities. The most common of these “simplified” approaches are briefly outlined below.

2.1 Guinier’s approximation

For a dilute system of randomly oriented particles with similar sizes, Guinier has shown that the smallest angles within the scattering curve can be approximated to a Gaussian function:

$$I(q) = I(0) e^{-q^2 R_g^2/3} \quad (9)$$

where R_g is the so-called gyration radius and $I(0)$ is scattering intensity extrapolated at zero angle. The gyration radius is defined as analogous to the radius of inertia in mechanics with the difference that here the electrons of the former substitute the mass elements of the latter. Though R_g cannot completely describe the geometry of a particle, its value is precisely known for simple geometrical shapes. For example, the radius of gyration of an ellipsoid particle is a function of the three semi-axis lengths according to $R_g^2 = (a^2 + b^2 + c^2)/5$ (so that for spheres of radius R , it will be simply $R_g = \sqrt{3/5}R$). Thus, equation 9 will readily yield a reckoning of the average particle dimension for groups of particles with a similar shape and size.

The scattering intensity at zero angle is related to concentration, contrast and average particle volume V_P , according to

$$I(0) = nV_P^2(r_e\Delta\rho)^2. \quad (10)$$

Such parameters can be derived from $I(0)$ if data have been expressed in so-called absolute units (usually cm^{-1}). More in detail, detector counts C_{ij} in the ij pixel associated to the \mathbf{q}_{ij} scattering vector are transformed in absolute scale by

$$I(\mathbf{q}_{ij}) = \frac{C_{ij}}{\Phi_0 \varepsilon_{ij} A_{ij} t D T \Delta\Omega_{ij}} \quad (11)$$

where: Φ_0 is the incident flux of photons (photons/s/cm²), ε_{ij} the pixel efficiency factor, A_{ij} the pixel area (cm²), t the measurement time (s), D the sample thickness (cm), T the transmission factor of the sample and $\Delta\Omega_{ij}$ (sr) the solid angle seen by the ij pixel in the direction 2θ .

The angular region where the Guinier’s approximation applies depends on the particle size through the usual law of reciprocity and is typically determined by the inequality $qR_g \leq 1.3 \div 1.8$ [3]. This region can be easily visualized by checking

the linearity of the logarithm of $I(q)$ as a function of q^2 , a graph called "Guinier's plot". From the intercept and the slope of this plot the values of $I(0)$ and R_g can be obtained, respectively. Two populations with different particle sizes may give rise to two distinct Guinier's regions. Yet, if the distribution of particle sizes is broad, their different contributions smear out the curve and dimensions are then difficult to determine.

2.2 Porod's law

On the other side of the angular range (high q region), we find that, in most cases, the data follow an asymptotic behaviour with a fourth power-law decay. In this case, the product $q^4 I(q)$ tends to settle on a constant value. Porod showed that this is to be expected for a so-called two-phase systems and demonstrated the following equation:

$$I(q) = (r_e \Delta \rho)^2 \frac{2\pi S}{q^4} \quad (12)$$

where S is the total surface of the interface between the two phases divided by the scattering volume. Moreover, possible oscillations shown by the curve when reaching the asymptotic value provide information on the angularity of the interface (be it a smooth or sharp-edged surface) [4, 5]. Situations that deviate from Porod's law have been explained by the presence of a so-called smooth interface, in other words, a gradual change from ρ_P to ρ_0 , or by fractality (see below). Porod's approach is particularly important because we need not assume a dilute system, implying that it is appropriate to densely packed particles as well. In fact, scattering due to inter-particles distances (structure factor) is depressed at these angles. The angular range attained by the asymptotic value depends on the particular sample studied and, under certain circumstances, even two distinct Porod's regimes for two distinct particle populations may be identified.

2.3 The scattering power

Porod also demonstrated that the integral of the scattering intensity (expressed in absolute-scale) over the entire \mathbf{q} -space depends on the mean square fluctuation of the electron density $\rho(\mathbf{r})$ of the entire system around its average value:

$$\int I(\mathbf{q}) d\mathbf{q} = (2\pi)^3 r_e^2 \langle [\rho(\mathbf{r}) - \langle \rho(\mathbf{r}) \rangle]^2 \rangle . \quad (13)$$

This equation is valid for any system, oriented or disordered, diluted or densely packed and also when it is not possible to recognize a true particle, for example in

fractal structures. For a two-phase and isotropic system, Eq. 13 transforms to the so-called “scattering power” or “Porod’s invariant”,

$$Q = \int_0^\infty q^2 I(q) dq = 2\pi^2 \eta(1-\eta)(r_e \Delta\rho)^2 \quad (14)$$

where η and $(1-\eta)$ are the volume fractions of the phase with electron density ρ_P and ρ_0 , respectively. The quantity may be calculated if the experimental data can be extrapolated to zero and infinity by applying Guinier’s approximation and Porod’s law, respectively. Thus, if the volumetric fraction is known, the difference in electron densities can be obtained, and vice versa.

For a dilute system of particles ($1-\eta \approx 1$), the Porod’s invariant transforms to

$$Q = 2\pi^2 n V_P (r_e \Delta\rho)^2. \quad (15)$$

By combining this equation with Eq. 10, the average particle volume V_P can be derived even if the contrast is unknown, $V_P = 2\pi^2 I(0)/Q$. However it should be borne in mind that if the particle surface is not sharp-edged, such as for biological macromolecules or for disordered chains, the behaviour of the scattering intensity at high q does not follow the Porod’s law and the values of V_P calculated from the Porod’s invariant can strongly deviate from the correct value [3, 6]. For porous systems, Eq. 15 can be combined with Eq. 12 (Porod law), to obtain the specific surface area $\sigma_P = S/(nV_P)$, a key parameter which is usually measured by adsorption methods, like the Brunauer, Emmett and Teller (BET) method. A comparison with the latter method, however, needs to take into account that, differently from BET, SAXS measures both open and closed pores.

2.4 Debye’s approximation and Kratky plot

Disordered polymeric chains distributed over many conformations, such as unfolded proteins, can be studied with the SAXS technique. The simplest statistical description of an infinitely thin chain formed by identical monomers separated by a fixed distance b is the “random-walk” or “Gaussian-chain” model: the position of a monomer can be in any point of the space provided the distance from the previous monomer of the chain is b . The form factor of a randomly oriented Gaussian-chain is expressed by the Debye’s law,

$$P_{GC}(q) = (r_e \Delta\rho)^2 V_P^2 \frac{2}{\phi^2} (e^{-\phi} + \phi - 1) \quad (16)$$

where $\phi = q^2 R_g^2$. The asymptotic behaviour of this equation is q^{-2} . Hence, by reporting experimental scattering intensity in the form of Kratky plot, $q^2 I(q)$ vs. q , the graph shows a constant value at high q , as shown in Fig. 3, blue curve. On the contrary, globular shapes show a Kratky plot with a typical large peak. For the law

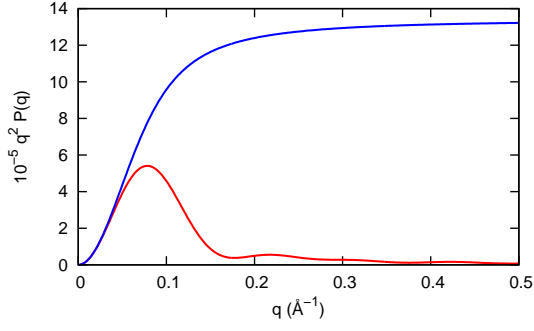


Fig. 3 Kratky plots of the form factors of randomly oriented compact and disordered shapes. Red curve: ellipsoid (Eq. 6: $r_e \Delta \rho = 3 \cdot 10^{-6} \text{ \AA}^{-2}$, $a = 30 \text{ \AA}$, $b = c = 20 \text{ \AA}$; blue curve: Gaussian chain with $R_g = 18.4 \text{ \AA}$ and the same contrast and volume of the ellipsoid.

of reciprocity, the larger the radius of gyration the smaller the value of q where the peak is centered (Fig. 3, red curve). It is evident that a simple representation of the scattering intensity in the form of a Kratky's plot can provide at first glance basic information on the compactness of the particles.

2.5 Distance distribution function

An other relevant information which can be drawn from the data for a two-phase system of randomly oriented particles is the distance distribution function $p(r)$, connected to the scattering intensity by means of an isotropic Fourier transform

$$p(r) = \frac{2r}{\pi} \int_0^{\infty} dq I(q) q \sin(qr), \quad (17)$$

and the scattering intensity is the inverse Fourier transform of $p(r)$,

$$I(q) = \int_0^{D_{\max}} p(r) \frac{\sin(qr)}{qr} dr. \quad (18)$$

$p(r)$ represents the probability distribution to find within the particle volume two points at distance r . It is a bell-shaped function, which reaches zero at the maximum particle diameter D_{\max} . The “direct” calculation of $p(r)$ via Eq. 17 requires to extrapolate data at low and high q with Guinier and Porod approximation, respectively. This approach can lead to wrong results, in particular when the experimental q -range is far from the Porod regime q^{-4} or when particles have smooth surfaces. In these circumstances it is preferable to use “indirect” methods, such as GIFT [7] or GNOM [8], where the $p(r)$ is written as a linear combination of elementary functions, such as cubic B splines. The unknown parameters of the linear combination are optimized by fitting the $I(q)$ calculated with Eq. 18 to the experimental scattering intensity. Regularization procedures can also be applied in order to control the balance between the goodness of fit and the smoothness of the $p(r)$.

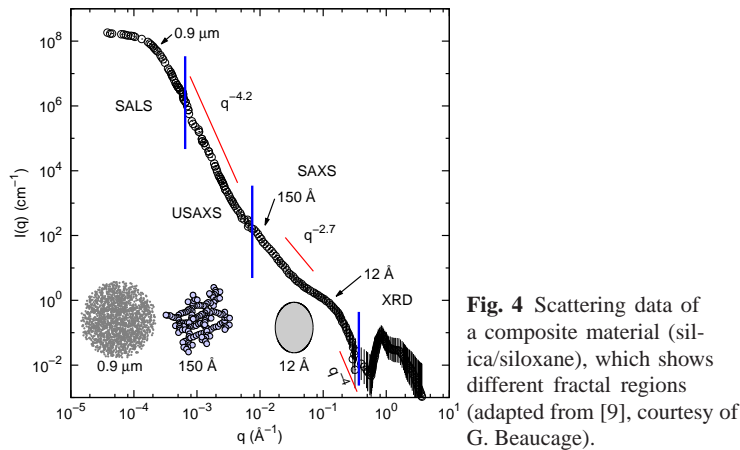


Fig. 4 Scattering data of a composite material (silica/siloxane), which shows different fractal regions (adapted from [9], courtesy of G. Beaucage).

2.6 Fractality

The fractal dimension of a system is readily assessed through small angle scattering measurement. Scale invariance, the main characteristic of fractal systems, is mirrored in the small angle scattering intensity as a decay in the power-law. In turn, the value of the power-law is directly related to the fractal dimension, and a value of -4 (Porod's law, Eq. 12) is expected for a non-fractal system. Therefore, we need only plot the data in bi-logarithmic scales and check for linearity in the curve. The angular region where linearity lies indicates the dimensional range in which the system is fractal; the slope provides its fractal dimension. Slope changes indicate structural level changes. Fig. 4 is an example of small angle data in a very wide angular range. Measurements taken with different experimental apparatuses have been joined in order to investigate the structure of silica/siloxane, a composite ceramic/polymeric material with a very large range of dimensional scales. The schematic drawings below the curve describe the different fractal objects concerned and their correspondence to angular regions of different slopes. Small angle light scattering (SALS) indicates the presence of globular clusters on a micrometer scale (the change in slope occurs at q with a corresponding value of $0.9 \mu\text{m}$). At wider angles, SAXS reveals the fractal nature of the structure down to approximately 15 nm. The linear region with a slope of -4.2 describes the internal organization of the globular clusters. At sizes of approximately 1.2 nm, the structure is once again fractal, but with a different fractal dimension (slope -2.7), which reveals the basic units of the fractal structure. The last linear part of the data, before the peaks of X-ray diffraction (XRD) come into play, has a -4 slope characteristic of Porod's law.

3 Experimental

SAXS is usually measured in transmission geometry: a monochromatic X-ray beam strikes the surface of the sample perpendicularly and the scattering is collected by a detector placed behind the sample. In this experimental configuration, a signal of a significantly lower intensity than that of the transmitted beam must be measured as close as possible to it. The higher the resolution² requested, the smaller the incident beam must be. Unfortunately, resolution increases linearly with decreasing the beam size, whereas the corresponding decline of intensity is much more rapid. Thus, special apparatuses must be devised for small angle scattering experiments, in order to reduce the transmitted beam size without compromising its intensity. However the sensitivity and resolution in a SAXS experiment are intrinsically limited by the quantity of photons emitted by the X-ray source.

In 1969, Guinier, one of the inventors of small angle scattering, expressed his concerns by articulating his thought as follows [10]

From the experimental point of view [...], small angle scattering appears to have reached a steady value. The apparatus for small angle scattering will certainly be continuously improved but *no major change can be foreseen, unless the power of X-ray sources is increased by a factor 10 or 100*, which is rather unlikely.

Then synchrotron arrived, and Guinier's pessimistic expectations were proven unwarranted. At the synchrotron source at ESRF (Grenoble, France), X-ray beams with a brilliance 10^{12} higher than those of conventional laboratories were produced! With such intensities devices as monochromators that improve the quality of the incident beam or converging mirrors or microcapillaries that change beam characteristics could now be used despite their absorbing part of the radiation. Sufficient transmitted intensity could be obtained by using soft X-rays. An enormous increase in the distance of the sample-detector was now feasible (12 m at the USAXS line in Hamburg, 56 m from the source!) and two-dimensional detectors could be routinely used.

The dramatic increase in the beam intensity has cleared the way for a series of measurements that were formerly impossible to obtain:

1. *Time-resolved measurements*: Newly developed detectors with greater efficiency also make it possible to collect statistically significant data in seconds and, under certain circumstances, even in milliseconds [11]. Thus the kinetics of such processes as heating, stretching, oxidation, and reduction may be followed *in situ*.
2. *Space-resolved measurements*: Different devices have been developed to obtain beams with sections in the micron, or even sub-micron range, and thus map samples that are not spatially homogeneous by using small angle scattering.
3. *Reflection measurements*: In order to study the surface of thin layers, measurements may be taken at a grazing incidence that is smaller than the critical angle

² In the context of SAXS the term 'resolution' is used as a synonym for 'smallest measurable angle' $2\theta_{min}$, which in turn corresponds to the *largest* measurable object D_{max} . Either $2\theta_{min}$ or D_{max} are used to indicate the attainable resolution. Note that the usage made by microscopists or spectroscopists is different. There, resolution stays for the *smallest* detail that can be appreciated.

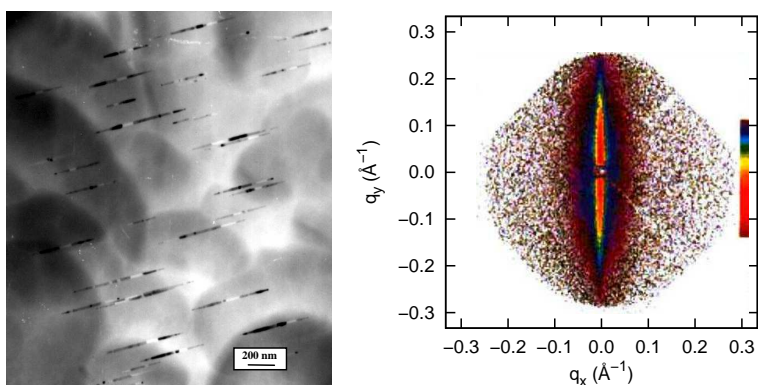


Fig. 5 Electron microscopy (left) and SAXS two-dimensional pattern (right) of a polarising glass containing needle-like silver crystals. The comet-like figure on the SAXS data is the beam-stop with its support.

for total reflection (GISAXS). In this situation, the information stems solely from the surface layer of the sample. With a two-dimensional detector, information on lateral correlation, as well as on the depth profile, can be gathered.

4. *Anomalous scattering (ASAXS)* (also known as resonant or contrast variation): Synchrotron sources have a unique feature that allows the researcher to choose, at will and with continuity, the wavelength to be used in the measurement. ASAXS exploits the very small variation in one part of the atomic scattering factor when the energy of the X-ray is close to the absorption edge of that particular atomic element. By subtracting the scattering obtained at two different energies near the edge, the scattering resulting from that particular element may be isolated, making SAXS an atom-selective technique [12].

4 Case studies

The following describes some exemplary experimental cases that exploit synchrotron light³. These measurements could not have been carried out with conventional laboratory equipment.

Polarising glass

These are types of aluminoborosilicate glass in which well dispersed spherical Ag(Br,Cl) crystallites are allowed to grow inside the glass matrix by means of a thermal treatment. They are then heated above their softening temperature, and drawn.

³ For a complete list of SAXS beamlines see under "SAXS" in Wikipedia.

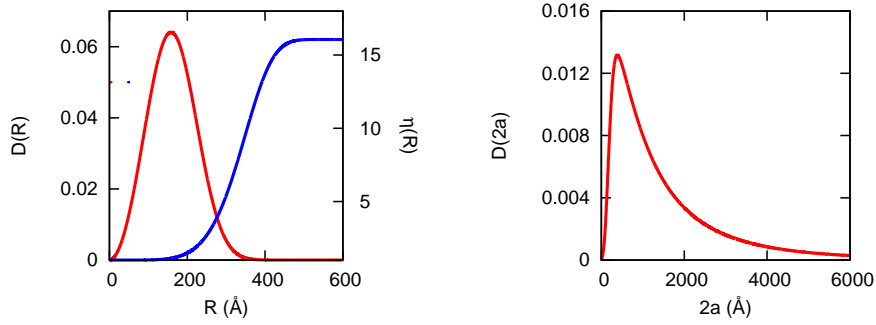


Fig. 6 Left: The distribution of radii $D(R)$ of the crystalline particles before the drawing and the elongation function $\eta(R)$. Right: The resulting length distribution $D(2a)$ of the elongated particles.

In this way, the softened spherical crystallites lose their shape and transform into needle-shaped crystalline particles that are perfectly parallel to the surface and oriented in the direction of their stretching. A reduction in hydrogen transforms the silver halide into silver and turns the glass into a highly effective polarising material. This material represents a perfect example of the situation previously described under Sect. 1.3.2, paragraph “Dilute systems”. In Fig. 5, a TEM image and a SAXS measurement of such a glass are shown [13, 14]. The two-dimensional analytical Fourier transform of a distribution of ellipsoidal particles can be fitted to the experimental data in order to determine the particle size distribution (the minor and major axes of the ellipsoidal particles). With the two-dimensional fit, data may be extrapolated into the blind zone of the beam-stop in order to obtain information on much larger particles than the resolution of the instrument would otherwise allow. Rough average values for the major and minor axes could be more simply obtained by applying Guinier’s approximation to sections of the data along the major and minor axes of the pattern. Yet, the two-dimensional pattern allows us to glean not only the complete distribution, but also information on the drawing process. Its description may be introduced into a mathematical model, where the original distribution of spheres is elongated according to a given function based on fluid-dynamical considerations (see Fig. 6). The crystallite size distribution before stretching as well as the value of surface energy of the silver halide phase (from one of the parameters of the elongation function) can be obtained by using this model. By comparing the glasses before and after their chemical reduction, it was found that the loss of Cl and Br atoms during chemical reduction causes a re-arrangement of silver atoms inside the glass cavities containing the elongated particles. The glassy matrix is, in fact, rigid at the temperature at which the chemical reduction occurs, while silver halide approaches its melting point. Silver particles are rearranged inside glass cavities into two or three shorter sub-particles separated by empty regions. Voids constitute approximately two thirds of the total volume of the cavities. However, the polarising optical properties correlate well with dimensions of cavities. This is because the di-

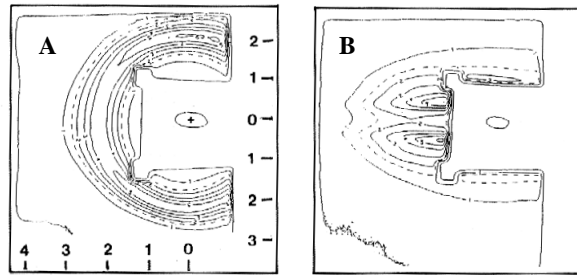


Fig. 7 SAXS patterns of an SBS polymer in a time-resolved drawing experiment: before (A) and during stretching (B). A rectangular beam-stop is visible in the center.

mensions of voids are much smaller than the wavelength of visible and near-infrared light and represent just a small perturbation to the global effect caused by silver.

Drawn polymers

During solidification of the styrene-butadiene-styrene (SBS) block co-polymer, a synthetic rubber mainly used for shoe soles, the long, folded polymer chains organize into semi-crystalline domains of one component regularly dispersed in the other amorphous one. The crystalline phase is rigid, whereas the amorphous one is flexible, thus imparting to this material its interesting properties. Which of the two components will crystallize and the shape that the rigid domains assume mainly depend on the composition. SAXS measurements of these samples [15, 16] (Fig. 7A) show isotropic patterns with a rather intense ring and two less intense peaks at distances with precise ratios between them: $1 : \sqrt{7}$ and $1 : \sqrt{3}$. These values are indication of a locally hexagonal structure, while peak positions indicate a mean distance between particles of about 45 nm. This is the case in the Sect. 1.3.2, paragraph “Densely packed systems”, that is, randomly oriented particles of unknown shape at close regular distances. The presence of peaks at regular distances and with decreasing intensities reveal the existence of a structure factor $S_M(\mathbf{q})$, as described in Eq. 7. Yet, since the material is capable of being deformed, we may obtain further information by looking at changes in the small angle scattering when the material is stretched. In Fig. 7B, the pattern drastically changes: an ellipsoidal background is modulated by two “linear” peaks perpendicular to the stretching direction. The distance between these two peaks decreases when the draw ratio increases. Here, the cylindrical domains orient in the direction of the stretching, and the distance between them steadily increases. This situation is similar to that of the polarising glasses discussed above, with the additional factor of a maximum due to the regularity in the distance among the densely packed particles. The shape and dimension of the styrene domains can now be determined from the evaluation of the ellipsoidal background. This information was missed in the unstretched sample because of the average over all randomly oriented domains.

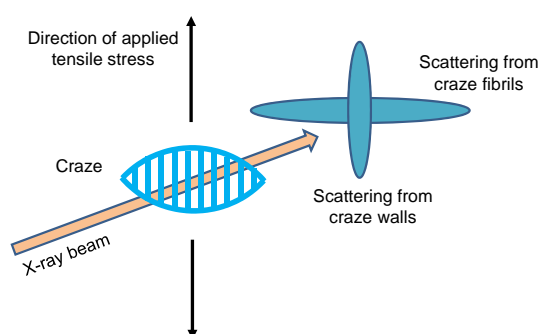


Fig. 8 Schematic sketch of the structure of crazes and their SAXS pattern (adapted from [17], courtesy of M.A. Singh).

Fibril crazes

The plastic deformation process of many polymers is accompanied by the formation of fibril crazes, *i.e.* micron-scale cracks that are bridged by filaments of polymer. Crazes are oriented 90° to the applied stress, while fibrils are parallel to it. Fibrils can absorb up to 90% of the deformation energy, even though, in some cases, they can develop into pure cracks, a precursor to failure. These structures are often oblate ellipsoids, 50-100 μm long and 0.1-2 μm large, and are grooved by hundreds of different parallel fibrils, 20-30 nm apart and with a diameter of 5-30 nm. The formation of fibrils gives rise to a cross-shaped SAXS pattern that is actually a superposition of the scattering due to the shape of the structure (a void) on the one resulting from the perpendicular fibrils (see Fig. 8). Quantitative analysis of these scattering patterns can provide precise information on the dimension of crazes and on their inner structure. Using a synchrotron source, the process of plastic deformation can be followed *in situ* with a time-resolved measurement, and the formation and growth mechanisms studied.

Metal supported catalysts

Most heterogeneous catalysts consist of metal particles well dispersed in a porous matrix. Because these metals are costly, their use must be optimized. The process of catalysis occurs on the surface of metal particles, therefore optimization is obtained by maximizing the surface/volume ratio. Since this ratio increases as the size of the particle decreases, chemical engineers strive to obtain well-dispersed (*i.e.* not agglomerated) nanoparticles. In principle, SAXS is an ideal technique for determining particle size at this scale; however, pores in the matrix usually cause a very high scattering intensity that hides or interferes with the scattering intensity of the metal phase. Anomalous small angle scattering inherently allows one to remove this unwanted scattering. By using synchrotron radiation, the incident beam energy can be tuned close to the metal absorption edge where the scattering of the metal has a small, but detectable, dependence on energy (see Fig. 9) while the scattering of the

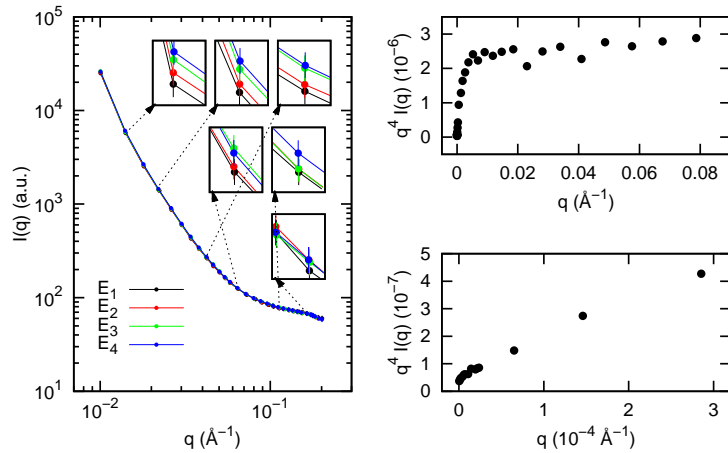


Fig. 9 Left: The scattering of a gold catalyst, dispersed in porous carbon. Note in the insets the minimal difference in the SAXS signals at different energies. Right: A Porod's plot of the SAXS signal. Two Porod's regions are found, which indicate the presence of two populations of particles (the innermost Porod's region does not tend towards a constant because of an overlap in the scattering of the two populations of particles).

matrix is constant [18, 19]. By subtracting the scattering of two measurements at different energies, we can isolate the scattering of the metal.

This technique is even more powerful in the case of bi-metallic catalysts, because the two metals can be selectively investigated by tuning the energy to the two absorption edges. In this way, we can determine if the two metals form an alloy, different particles, or two-phase particles (where the core of one metal covers the other with a shell). In the case of Fig. 9, ASAXS revealed that the greater part of the metal forms 1-2 nm particles. Diffraction measurements could only detect a second population of larger particles (14 nm) that are significantly less active in the catalytic process.

Spatial resolution: Micro and Nanofocused beamlines

The availability of micrometric beams with sufficient intensity at synchrotron laboratories has made the spatial resolution of inhomogeneous materials, such as bones, cartilage, or wood, possible. At the nanometer scale, bone and mineralized cartilage consist of small mineral particles embedded in an organic matrix (collagen). For bone, these particles are known to be needle- or plate-shaped with an average thickness of about 3 nm and a length of a few hundred nanometers [20]. One of the first researches using a microbeam [21] showed that it is possible to use SAXS to investigate the different structures of contiguous zones inside a human vertebra and distinguish the different orientations assumed by the mineral particles in different

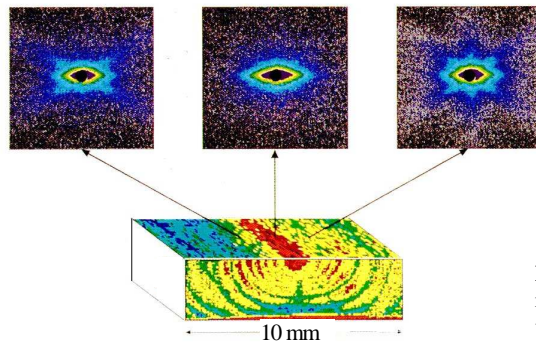


Fig. 10 Example of spatially resolved SAXS of a human vertebra specimen [21] (courtesy of P. Fratzl).

positions of the bone (Fig. 10). By using the integrated intensity of each individual SAXS pattern, a sort of orientation-sensitive map of the sample can be composed that is complementary to radiography. The spatial resolution achieved in that experiment at ELETTRA (Trieste, Italy) was $200\ \mu\text{m}$. Nowadays, dedicated microfocused beamlines can obtain resolution in the microns or even sub-microns range and the new Nanofocused extension of the ID13 beamline at ESRF (Grenoble, France) promises to have a beam size of 50 nm or less.

Shape determination of solution proteins: the proteomics era

'Proteomics' is a new subject in molecular biology aimed to study structure and function of all the proteins coded in the genome of a cell. Most of those proteins are unknown and only a fraction of them can be crystallized and then investigated by X-ray crystallography. SAXS is one of the most suitable technique to determine the structure of non-crystallizable proteins. In this framework, the actual policy of synchrotrons is to dedicate to biology SAXS beamlines specifically conceived to get an high-throughput of protein structures [22, 23]. Such Bio-SAXS beamlines (such as BM29 at ESRF [24]) equipped with automated data collection aimed to minimize the volume of the biological samples to a few tens of microliters.

The main objective that proteomics demands to synchrotron SAXS is to get the shape of compact proteins in solution. A lot of effort has been put to develop methods and related software able to reconstruct the 3D shape of monodisperse proteins from their 1D SAXS profiles. The first approach was based on the description of the protein envelope as a linear combination of spherical harmonics [26, 27], a method later improved by the implementation of group theory and maximum entropy concepts to deal with protein symmetry [25]. In Fig. 11 the shape of the carboxypeptidase enzyme from *Sulfolobus solfataricus* (CPSO) obtained by a SAXS curve recorded at the ELETTRA synchrotron (Trieste, Italy) is shown [28]. Results have confirmed the tetrameric structure provided by a structural alignment of a template. In an other class of shape reconstruction methods (DAMMIN [29], DALAI_GA [30]) the protein structure is obtained by finding the best combination

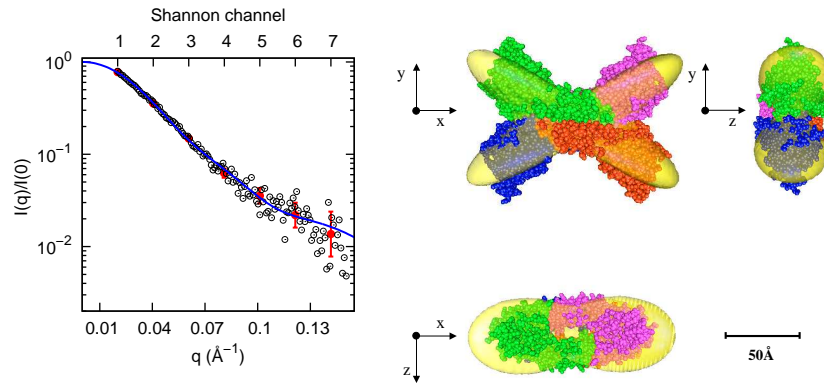


Fig. 11 Shape-reconstruction based on MPOLE method [25]. Left: the blue solid lines is the best fit of the experimental SAXS curve (black open points) related to seven Shannon channels (red close points). Right: reconstructed shape (yellow envelope) of the CPSO tetramer superimposed to the computer designed model (full atoms representation).

of densely packed identical spheres whose unique diameter is adjusted to match the experimental resolution. The compactness of the protein is taken into account by introducing penalty terms in the search algorithm. An example of shape reconstruction obtained with DAMMIN is shown in Fig. 12 [31].

The most recent methods, such as GASBOR [32], are based on the best arrangement of connected spheres representing the amino acids sequence of the protein and include constraints for avoiding steric clashes and for promoting compactness.

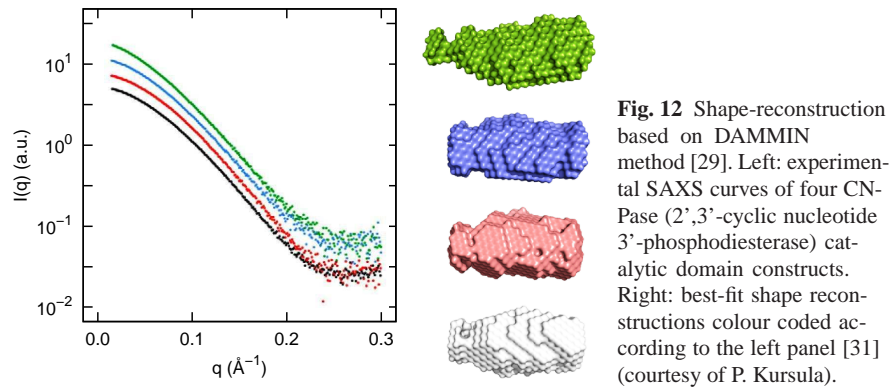


Fig. 12 Shape-reconstruction based on DAMMIN method [29]. Left: experimental SAXS curves of four CN-Pase (2',3'-cyclic nucleotide 3'-phosphodiesterase) catalytic domain constructs. Right: best-fit shape reconstructions colour coded according to the left panel [31] (courtesy of P. Kursula).

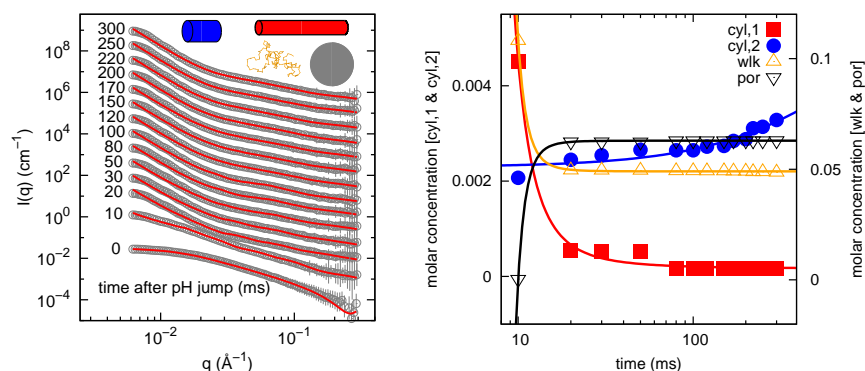


Fig. 13 Left. SAXS curves of the apomyoglobin W7FW14F mutant (10 gL^{-1} concentration) measured at different times (reported beside each curve) after pH jumps from 4 to 7. Solid lines represent the best fits to the data. Right. Molar concentrations of the four species obtained by fitting SAXS data and expressed as a function of the time after the pH-jump.

Time-resolved study of amyloid fibrils

'Amyloids' are stable, ordered, filamentous aggregates of proteins or peptides that arise from an anomalous folding of the amino acid chain. A broad range of human neuro-degenerative diseases (such as Parkinson's or Alzheimer's diseases) are caused by the deposition of amyloid fibrils. Within the broad field of amyloid research, a key issue is the description of the fibrillogenesis pathway at a molecular level, in particular the study of the early aggregation events. Amyloid research has also shown that any protein, in particular circumstances, can undergo a conformational change that lead to amyloid formation [33]. Time-resolved SAXS is of pivotal importance to gain information on the intermediate structures that form at the beginning of the amyloid fibrillar process, in the millisecond time range. In a recent study, a mutant of apo-myoglobin, which forms amyloid fibrils when pH is varied from 4 to 7, has been investigated with time-resolved SAXS [11]. SAXS curves for different times after the pH-jump are shown in Fig. 13. The whole set of curves has been analysed by using a unique model that combines four form factors: one unfolded protein monomer ('worm-like' model, code as wlk in Fig. 13), two cylinders representing the prefibrillar oligomeric species (cyl,1 and cyl,2) and a very large assembly described by the Porod's law (por). Results indicates that in less than 20 ms after the pH jump the first fibrillar species appear.

References

1. D.B. Williams, C.B. Carter, *Transmission Electron Microscopy* (Plenum Press, 1996)
2. H. Hartmann, A. Bongers, H. Decker, T. Nawroth, G. Goerigk, in *HasyLab Annual Report 1998* (1998)

3. L.A. Feigin, D.I. Svergun, *Structure analysis by small-angle X-ray, neutron scattering* (New York, Plenum Press, 1987)
4. S. Ciccariello, G. Cocco, A. Benedetti, S. Enzo, *Phys. Rev. B* **23**, 6474 (1981)
5. S. Ciccariello, A. Benedetti, *Phys. Rev. B* **26**, 6384 (1982)
6. P.V. Konarev, V.V. Volkov, A.V. Sokolova, M.H.J. Koch, D.I. Svergun, *J. Appl. Cryst.* **36**, 1277 (2003)
7. A. Bergmann, G. Fritz, O. Glatter, *J. Appl. Cryst.* **33**, 1212 (2000)
8. D.I. Svergun, *J. Appl. Cryst.* **25**, 495 (1992)
9. G. Beaucage, T.A. Ulibarri, E.P. Black, D.W. Schaefer, in *Organic Hybrid Materials*, vol. 585, ed. by J.E. Mark, C. Lee, P. Bianconi (ACS. Symp. Series, 1995), chap. 9, pp. 97–111
10. A. Guinier, *Physics Today* **22**, 25 (1969)
11. M.G. Ortore, F. Spinozzi, S. Vilasi, I. Sirangelo, G. Irace, A. Shukla, T. Narayanan, R. Sini-baldi, P. Mariani, *Phys. Rev. E* **84**, 061904 (2011)
12. S. Polizzi, P. Riello, G. Goerigk, A. Benedetti, *J. Sync. Rad.* **9**, 65 (2002)
13. S. Polizzi, P. Riello, G. Fagherazzi, M. Bark, N.F. Borrelli, *J. Appl. Cryst.* **30**, 487 (1997)
14. S. Polizzi, P. Riello, G. Fagherazzi, N.F. Borrelli, *J. Non-Cryst. Solids* **232-234**, 147 (1998)
15. S. Polizzi, N. Stribeck, H.G. Zachmann, R. Bordeianu, *Colloid. Polym. Sci.* **267**, 281 (1989)
16. S. Polizzi, P. Bösecke, N. Stribeck, H. Zachmann, R. Zietz, R. Bordeianu, *Polymer* **31**, 638 (1990)
17. G.J. Salomons, M.A. Singh, T. Bardouille, W.A. Foran, M.S. Capel, *J. Appl. Cryst.* **32**, 71 (1999)
18. A. Benedetti, S. Polizzi, P. Riello, F. Pinna, G. Goerigk, *Journal of Catalysis* **171**, 345 (1997)
19. A. Benedetti, L. Bertoldo, P. Canton, G. Goerigk, F. Pinna, P. Riello, S. Polizzi, *Catalysis Today* **48**, 485 (1999)
20. P. Fratzl, M. Groschner, G. Vogl, H.J. Plenck, J. Eschberger, N. Fratzl-Zelman, K. Koller, K. Klaushofer, *J. Bone Miner. Res.* **7**, 329 (1992)
21. P. Fratzl, H. Jakob, S. Rinnerthaler, P. Roschger, K. Klaushofer, *J. Appl. Cryst.* **30**, 765 (1997)
22. G.L. Hura, A.L. Menon, M. Hammel, R.P. Rambo, F.L. Poole, S.E. Tsutakawa, F.E. Jenney, S. Classen, K.A. Frankel, R.C. Hopkins, S.J. Yang, J.W. Scott, B.D. Dillard, M.W. Adams, J.A. Tainer, *Nature Methods* **6**, 606 (2009)
23. T.D. Grant, J.R. Luft, J.R. Wolfley, H. Tsuruta, A. Martel, G.T. Montelione, E.H. Snell, *Biopolymers* **95**, 517 (2011)
24. P. Pernot, A. Round, M. Brennich, Bm29: Biosaxs beamline (2013). URL http://www.esrf.eu/UsersAndScience/Experiments/MX/About_our_beamlines/BM29
25. F. Spinozzi, F. Carsughi, P. Mariani, *J. Chem. Phys.* **109**, 10148 (1998)
26. D. Svergun, H. Stuhrmann, *Acta Crystallogr.* **A47**, 736 (1998)
27. D.I. Svergun, V.V. Volkov, M.B. Kozin, H.B. Stuhrmann, C. Barberato, M.H.J. Koch, *J. Appl. Cryst.* **30**, 798 (1997)
28. E. Occhipinti, P. Martelli, F. Spinozzi, F. Corsi, C. Formantici, L. Molteni, H. Amenitsch, P. Mariani, P. Tortora, R. Casadio, *Biophys. J.* **85**, 1165 (2003)
29. D.I. Svergun, *Biophys. J.* **76**, 2879 (1999)
30. P. Chacón, J.F. Díaz, F. Morán, J.M. Andreu, *J. Mol. Biol.* **299**, 1289 (1999)
31. M. Myllykoski, A. Raasakka, H. Han, P. Kursula, *PLoS one* **7**, e31852 (2012)
32. D.I. Svergun, M.V. Petoukhov, M.H.J. Koch, *Biophys. J.* **80**, 2946 (2001)
33. J. Schnabel, *Nature* **464**, 828 (2010)

Further Reading

1. O. Glatter, O. Kratky, *Small angle scattering X-ray* (Academic Press, London, 1982)
2. A. Guinier, G. Fournet, *Small angle scattering of X-ray* (Wiley, New York, 1955)
3. A. Guinier, *X-ray Diffraction* (W.H. Freeman and Co., San Francisco, 1963)
4. R. Hoseman, S.N. Bagchi, *Direct Analysis of Diffraction Methods* (North-Holland, 1962)
5. C.D. Putnam, M. Hammel, G.L. Hura, J.A. Tainer, *Q. Rev. Biophys.* **40**, 191 (2007)
6. B.R. Pauw, arXiv:1306.0637v1 **submitted** (2013)